Latent hardening and plastic anisotropy evolution in AA6060 aluminium alloy.

M. Khadyko[1,*], S. Dumoulin[2], G. Cailletaud[3] and O.S. Hopperstad[1]

[1] *Structural Impact Laboratory (SIMLab), Centre for Research-based Innovation, Department of Structural Engineering,*
Norwegian University of Science and Technology, NO-7491 Trondheim, Norway

[2]*SINTEF Materials & Chemistry, NO-7465 Trondheim, Norway*

[3] *MINES ParisTech, Centre des Matériaux, CNRS UMR 7633, BP 87 91003 Evry Cedex, France*

Abstract

The crystal plasticity theory predicts that hardening on a particular slip system and its corresponding work-hardening rate will depend on the slip activity on both this slip system and all others. The exact form of this dependence is defined by the latent hardening description in form of the latent hardening matrix or the interaction matrix. It has been assumed that this matrix describes the relative strength of various dislocation interactions and is therefore the same for a wide range of alloys with the same lattice structure. Different methods have been used to estimate the values of the interaction matrix components: one is experimental and uses strain-path changes; another simulates the dislocations dynamics in a crystal directly at the microscale and estimates the strength of the forming locks. In this work, the influence of the interaction matrix (and thus latent hardening) on the development of plastic anisotropy is studied. An extruded AA6060 alloy is tested in uniaxial tension in different directions and the anisotropy of the alloy is found to evolve considerably throughout the deformation. A crystal plasticity model is used to simulate the experimental tests, and the use of different interaction matrices is evaluated. A noticeable influence on the predicted evolution of plastic anisotropy as well as the stress-strain field and slip inside the constituent grains is found.

---

[*] Corresponding author: Mikhail Khadyko (mikhail.khadyko@ntnu.no)

1 Introduction

The mechanisms of plastic deformation of metallic materials at the microscale can be described by the crystal plasticity theory. Metals and alloys are crystalline materials and deform plastically by slip on specific crystallographic planes and directions denoted slip systems. The kinematics of this type of plastic deformation was first described by Taylor in [1, 2]. The plastic deformation accumulating on the slip systems leads to an increase in the resolved shear stress, i.e. the material work-hardens. The work-hardening in a crystal is particularly complex, because the slip resistance increases not only on the active but also on the non-active slip systems. The work-hardening of each slip system is therefore divided into self and latent hardening. The influence of latent hardening on the plastic deformation of a single crystal was observed already in [2], where the slip systems were activated or remained inactive depending not only on the orientation of the crystal but also on its deformation history. The response of a polycrystal depends on the properties of the constituent crystals and will also be affected by latent hardening. Therefore, predicting the properties of a polycrystal depends, among other things, on a good prediction of the latent hardening. This problem has been approached in different ways. The basic assumption that all non-active systems harden similarly was used in phenomenological models [3-5], where the self and latent hardening were described using two independent components. A more complex approach within the phenomenological framework was used in [6].

In [7] Taylor proposed a relationship between the resolved shear stress on the slip systems and the dislocation density in the crystal. It was combined with an equation that described the evolution of the dislocation density in [8] and [9], formulated for global stress and strain in the material. Later in [10] it was modified by accounting for dislocation densities on different slip systems. In this model, the dislocations interact with each other and get pinned on each other, forming different types of dislocation locks [11]. Depending on the relative position of the slip systems, these locks are divided into coplanar, collinear, Hirth (normal), glissile and sessile (Lomer-Cottrel) types. The relative strength of these locks combined together with the self-hardening, constitutes an interaction matrix with 6 independent components. This matrix in principle defines both the flow stress (i.e. the stress which is necessary to overcome the lock and to start the dislocation movement and plastic deformation) and the hardening rate – the stronger the lock, the more easily the dislocations get caught into it, contributing to the work-hardening. Teodosiu [10] used a very simple interaction matrix, based on the assumption that the self-hardening was negligible compared

to latent hardening, which was the same on all slip systems (a similar approach was used in [12] for modelling the plastic behaviour of copper).

The interaction between different slip systems and latent hardening were studied experimentally in [13, 14] and [15] on aluminium single crystals and in [16] on copper. The method used consisted in deforming the specimen in order to activate some specific slip systems, followed by a change in deformation path and then measuring the resistance on the other slip systems. The results were not very accurate or consistent with each other, probably due to the complexity of the experimental procedure. However, some general conclusions were made: the interaction matrix was reduced to 4 independent components, corresponding to different types of locks and these components were arranged from strongest to weakest. Coplanar, collinear and Hirth types were united under one value. These results were used in [17-20]. The model used in the latter treated the interaction matrix for flow stress and hardening differently. It was assumed that the flow stress is dominated by the averaged short-range interactions between dislocations and the interaction matrix in the strength expression was reduced to either one common coefficient or two – for self and latent hardening.

A new approach, which uses advances in computational mechanics, has been used to find the values of the interaction matrix components. It uses dislocation dynamics simulations, where the dislocations in a deforming crystal are modelled explicitly as moving, interacting linear defects in the lattice. In [21-23] the components of the interaction matrix were obtained by this method. The results were not consistent with [13]: the collinear interactions were shown to be much stronger than other types and merging coplanar, collinear and Hirth type interactions into one matrix component was shown to be unreasonable. Though these results were obtained under some strict assumptions (small strains, elastic constants and other material parameters for pure copper) they provide a way to estimate the interaction matrix for any face centred-cubic (FCC) metal.

In [24] the strain-path change approach was used again to try to find the interaction matrix of an FCC material in the light of these new results. Copper specimens were subjected to strain-path change (from pure shear to uniaxial tension) and the obtained stress-strain data were used to calibrate a model similar to the one proposed by Teodosiu [10, 25] and a phenomenological model relying on local hardening.

The crystal plasticity models have been known and used in the modelling of single crystals and polycrystals for a long time, thus the latent hardening has been also studied and a large volume of experimental results has been accumulated. However, what the actual latent hardening matrix (or interaction matrix) for any given material is still remains an open

question. The results obtained with different experimental and numerical procedures are quite different from each other. On the other hand, the obtained results are not tested on different kinds of loading conditions and materials. As stated above, the latent hardening is an important factor in the plastic deformation of a crystal and its influence should probably express itself in a variety of ways, not limited to the case of changing strain-paths.

In the present work, an experimental study is performed for an extruded aluminium alloy AA6060 in temper T4 with strong cube texture. Tensile tests are carried out in different material directions of the flat profile using cylindrical samples. The average true stress and the average true strain within the minimum cross-section are measured to failure. The experiments show that the anisotropy in flow stress and plastic flow is not constant but evolves considerably throughout the whole deformation process. To evaluate the influence of the interaction matrix (or latent hardening) on the predicted plastic anisotropy, these tests are modelled using the crystal plasticity finite element method (CP-FEM) with different interaction matrices and the predicted global response is compared to the experimental one. The local response at the level of the slip systems obtained in the CP-FEM simulations with different interaction matrices is also discussed.

The article is organised as follows. The mechanical tests on the extruded aluminium alloy AA6060 in temper T4 are described in Section 2. A review of the adopted crystal plasticity models is given in Section 3, while the finite element modelling is described in Section 4. The procedure of the calibration of the crystal plasticity models is presented in Section 5 using corrected data from the mechanical tests. Section 6 presents the results from the experimental and numerical studies and discusses the findings. Conclusions are provided in Section 7.

2   Experimental results

2.1   *Choice of the material and its microstructure*

The material, which was used as a model material, is the AA6060 aluminium alloy in T4 temper, delivered as an extruded flat profile with 10 mm thickness and 90 mm width. There are several reasons for choosing this alloy and heat treatment for this study. It is a recrystallized material with large equiaxed grains (see Figure 1), so that the influence of grain morphology on the material properties is small. The material is very ductile, so that the stress-strain curve for strains up to 140% may be obtained. The T4 temper corresponds to heating the material at 540°C in salt bath for 15 min, followed by water quenching and storage at

room temperature for prolonged time. This makes sure that Mg and Si, which are the primary alloying elements, are present in the alloy in form of solid solution and GP-zones/clusters, while precipitate particles are not formed during natural ageing. Depending on their size, the precipitates may act as a source for geometrically necessary dislocations during plastic deformation, in addition to the statistically stored dislocations [26], which cannot be described by the work-hardening rules adopted in this work.

The chemical composition of the alloy is given in Table 1. The material was analysed in the scanning electron microscope using electron back-scattering diffraction (EBSD) and EDAX TSL OIM software to provide grain morphology and texture. The grain morphology and the Orientation Distribution Function (ODF) are presented in Figure 1 and Figure 2, respectively. The EBSD measurements were carried out in the plane defined by the extrusion and normal directions of the profile, using 10 μm steps on a square grid. The ODF was calculated from the pole figures in the EDAX TSL OIM software using a harmonic series expansion and triclinic sample symmetry [27]. The total number of measured orientations (or grains) in the sample is 2611. The main component of the texture is a strong cube texture with a minor Goss component. Both the texture and the grain morphology are typical for recrystallized alloys.

2.2 Mechanical tests

The tensile specimens were obtained from the extruded flat profile at different angles θ to the extrusion direction with 22.5° interval (i.e., θ equals 0°, 22.5°, 45°, 67.5° and 90°). Three specimens were tested for each direction, giving a total of 15 tests. The specimen geometry is shown in Figure 3. A rectangular coordinate system xyz is defined such that the x-axis is in the transverse direction and the y-axis is in the longitudinal direction of the specimen, while the z-axis is always in the thickness direction of the extruded profile. Two laser gauges were measuring the diameters of the specimens in the width and thickness directions at high frequency during the tests, so the minimum diameters before and after necking are known with high accuracy. If we denote the measured diameters D_x and D_z, and assume that the deformed cross section is elliptical in shape (which is a reasonable assumption for an orthotropic material), then we may find the current cross-section area as

$$A = \frac{\pi}{4} D_x D_z \tag{1}$$

The true (Cauchy) stress is found as

$$\sigma_y = \frac{F}{A} \tag{2}$$

where F is the measured tensile force. If we also assume plastic incompressibility, the logarithmic strains may be expressed as

$$\varepsilon_x = \ln\left(\frac{D_x}{D_0}\right), \quad \varepsilon_y = \ln\left(\frac{A_0}{A}\right), \quad \varepsilon_z = \ln\left(\frac{D_z}{D_0}\right) \tag{3}$$

where D_0 and $A_0 = \frac{\pi}{4}D_0^2$ are the initial diameter and cross-section area of the specimen, respectively. The logarithmic strain is also used further in this work. The strain ratio is defined as

$$r_y = \frac{d\varepsilon_x}{d\varepsilon_z} \tag{4}$$

which equals unity for isotropic materials.

The results from the tensile tests are presented in Figure 4 and Figure 5. Figure 4a) presents representative true stress-strain curves to failure, whereas the scatter between parallel tests is displayed in Figure 4b). These results clearly demonstrate the anisotropic work-hardening of the AA6060 alloy. Figure 5a) presents the plastic flow in terms of the strain in the transverse direction of the tensile specimen as a function of the thickness strain. The thickness direction of the specimen always coincides with the thickness direction of the profile, while the width direction of the specimen is rotating and coincides with the width direction of the profile for the 0° orientation and with the extrusion direction for the 90° orientation. The strain ratio as function of tensile strain and tensile direction is plotted in Figure 5b). The anisotropy of the plastic flow is initially very strong but diminishes with tensile straining due to texture evolution. Since the results for the three specimens of each orientation are very close to each other, a representative curve for each orientation is shown and used further.

3 Constitutive modelling

3.1 Single crystal kinematics and kinetics

The finite deformation formulation is used. The total deformation of the crystal from the initial configuration Ω_0 to the current configuration Ω is mapped by the deformation gradient tensor $\mathbf{F}$, which may be multiplicatively decomposed into elastic and plastic parts [28]

$$\mathbf{F} = \mathbf{F}^e \mathbf{F}^p \tag{5}$$

where $\mathbf{F}^p$ maps the transformation between the initial configuration Ω_0 and the intermediate plastically deformed configuration $\bar{\Omega}$, and $\mathbf{F}^e$ maps the transformation from $\bar{\Omega}$ to Ω. Thus, $\mathbf{F}^p$ accounts for plastic slip and $\mathbf{F}^e$ accounts for elastic deformations and rigid body rotations. The slip systems in the initial and intermediate configurations are defined by vectors $\mathbf{m}_0^\alpha$ and $\mathbf{n}_0^\alpha$ — the slip direction and slip plane normal, respectively. These vectors are connected to the lattice and remain unchanged by $\mathbf{F}^p$, while $\mathbf{F}^e$ transforms them into current configuration vectors $\mathbf{m}^\alpha$ and $\mathbf{n}^\alpha$. Here α identifies the relevant slip system. The plastic velocity gradient in the intermediate configuration $\bar{\mathbf{L}}^p$ is defined as

$$\bar{\mathbf{L}}^p = \dot{\mathbf{F}}^p \left(\mathbf{F}^p \right)^{-1} = \sum_{\alpha=1}^n \dot{\gamma}^\alpha \mathbf{m}_0^\alpha \otimes \mathbf{n}_0^\alpha \tag{6}$$

where $\dot{\gamma}^\alpha$ is the slip rate on slip system α and n is the total number of slip systems (12 in the case of an FCC lattice). The elastic Green strain tensor $\bar{\mathbf{E}}^e$ in the intermediate configuration is defined as

$$\bar{\mathbf{E}}^e = \frac{1}{2} \left(\bar{\mathbf{C}}^e - \mathbf{I} \right), \quad \bar{\mathbf{C}}^e = \left(\mathbf{F}^e \right)^T \mathbf{F}^e \tag{7}$$

where $\bar{\mathbf{C}}^e$ is the elastic right Cauchy-Green deformation tensor and $\mathbf{I}$ is the unity tensor. The second Piola-Kirchhoff stress tensor $\bar{\mathbf{S}}$ in the intermediate configuration may be found from the Cauchy stress tensor $\boldsymbol{\sigma}$ as

$$\bar{\mathbf{S}} = \det \mathbf{F} \left(\mathbf{F}^e \right)^{-1} \boldsymbol{\sigma} \left(\mathbf{F}^e \right)^{-T} \tag{8}$$

This stress is power conjugate with the elastic Green strain tensor $\bar{\mathbf{E}}^e$ and may be found from the hyperelastic law

$$\bar{\mathbf{S}} = \bar{\mathbf{C}}_{el}^{\bar{S}} : \bar{\mathbf{E}}^e \tag{9}$$

where $\bar{\mathbf{C}}_{el}^{\bar{S}}$ is the tensor of elastic moduli. In the case of orthotropic symmetry it is defined by three independent components, describing the elastic anisotropy of the crystal.

The stress acting on the slip systems and power conjugate with the slip rate $\dot{\gamma}^\alpha$ is the resolved shear stress τ^α. It is found from the second Piola-Kirchhoff stress tensor as

$$\tau^\alpha = \bar{\mathbf{C}}^e \bar{\mathbf{S}} : \left(\mathbf{m}_0^\alpha \otimes \mathbf{n}_0^\alpha \right) \tag{10}$$

3.2 Flow and hardening rules

The flow rule used here is the well-known viscoplastic rule [29] which controls the activation of the slip systems

$$\dot{\gamma}^{\alpha} = \dot{\gamma}_0 \left(\frac{|\tau^{\alpha}|}{\tau_c^{\alpha}} \right)^{\frac{1}{m}} \text{sgn}\left(\tau^{\alpha} \right) \tag{11}$$

where $\dot{\gamma}_0$ is the reference slip rate, m is the slip rate sensitivity parameter and τ_c^{α} is the slip resistance of slip system α.

The Teodosiu-type hardening models use the dislocation density as the hardening parameter. Then the hardening of slip system α is described by an equation proposed in [7] and [10]:

$$\tau_c^{\alpha} = \tau_0 + a\mu b \sqrt{\sum_{\beta=1}^{n} d^{\alpha\beta} \rho^{\beta}} \tag{12}$$

where a is a dimensionless coefficient, μ is the elastic shear modulus, b is the length of the Burgers vector, ρ^{β} is the dislocation density on slip system β, and $d^{\alpha\beta}$ is the interaction matrix, showing the relative strength of interaction between the dislocations on slip systems α and β. The initial slip resistance τ_0 is assumed to be the same on all slip systems. The dislocation density ρ^{β} is assumed to have initially a negligibly small positive value. The dislocation density evolves according to [9, 10]

$$\dot{\rho}^{\alpha} = \frac{1}{b} \left(\frac{1}{K} \sqrt{\sum_{\beta=1}^{n} g^{\alpha\beta} \rho^{\beta}} - 2y_c \rho^{\alpha} \right) \left| \dot{\gamma}^{\alpha} \right| \tag{13}$$

where K is a dimensionless parameter that defines the accumulation of dislocations, y_c is the distance at which two dislocations with opposite Burgers vectors annihilate each other. $g^{\alpha\beta}$ is the interaction matrix, similar to $d^{\alpha\beta}$, but in this case the strength of dislocation interaction defines the accumulation of forest dislocations on slip system α depending on the dislocation density on system β. The total number of components in each of the interaction matrices $g^{\alpha\beta}$ and $d^{\alpha\beta}$ matrix is 144. The number of independent components is 6, corresponding to different types of the slip systems mutual orientations. The interaction matrix $g^{\alpha\beta}$ is given explicitly in Table 2; the interaction matrix $d^{\alpha\beta}$ has an analogous structure.

The phenomenological models describe work-hardening on slip systems with some convenient function. The latent hardening description is usually simpler than in the Teodosiu-type models and is limited to one matrix, connecting hardening rate with slip rate. As a typical example of the phenomenological model with this latent hardening description we consider the two-term Voce rule

$$\dot{\tau}_c^\alpha = \theta(\Gamma) \sum_{\beta=1}^{n} q_{\alpha\beta} \left| \dot{\gamma}^\beta \right| \tag{14}$$

where $q_{\alpha\beta}$ is the matrix of self-hardening and latent-hardening coefficients, and the accumulated slip Γ is defined by the evolution equation

$$\dot{\Gamma} = \sum_{\alpha=1}^{n} \left| \dot{\gamma}^\alpha \right| \tag{15}$$

The master hardening rate $\theta(\Gamma)$ is defined as

$$\theta(\Gamma) = \sum_{k=1}^{2} \theta_k \exp\left(-\frac{\theta_k}{\tau_k} \Gamma \right) \tag{16}$$

where θ_k and τ_k are material parameters. The initial slip resistance τ_{c0}^α is assumed equal for all slip systems.

In the numerical implementation of the single crystal plasticity model into the finite element method, one element may either represent a part of a grain (or possibly the whole grain) or it may represent many grains. In the latter case, the full-constraint Taylor method is used here to compute the element stresses. The full-constraint Taylor-type homogenisation assumes a constant deformation gradient throughout all the grains of a polycrystal, ignoring stress equilibrium, and the total stress is obtained as a simple average of the stresses in the grains:

$$\boldsymbol{\sigma} = \frac{1}{n_g} \sum_{g=1}^{n_g} \boldsymbol{\sigma}_g \tag{17}$$

where $\boldsymbol{\sigma}_g$ is the Cauchy stress in grain g, and n_g is the total number of grains. The grains are assumed to have equal volume.

4   Finite element modelling

The uniaxial tensile test was modelled using the finite element method. In all simulations the solid linear eight node "brick" elements with selectively reduced integration

were used. This type of finite elements is usually avoided in the context of crystal plasticity simulations. The main reason for this is that the actual grains or their representation with Voronoi tessellations are too complex to represent with a mesh consisting of regular hexahedra, so the grain volume and grain boundary shape will be only approximated, while the tetrahedral elements may represent them accurately. Still, as it was found in [30], the use of hexahedral elements in crystal plasticity simulations does not affect the global response of a modelled polycrystal. Considering the local response, the use of tetrahedral elements is necessary if the goal is to approximate a real polycrystal grain morphology as precisely as possible. On the other hand, if the goal is to model some representative polycrystal, e.g. consisting of equiaxed grains with similar volume, then the choice of element type is not as critical. The representation of grain boundaries in such models is usually rather simplified and abstract, and there is no evidence that the smooth grain boundary of tetrahedral mesh is substantially better than the jagged boundary of a hexahedral mesh in predicting the global stress-strain response. The hexahedral element also has an advantage of numerical efficiency. The linear tetrahedral elements give a noticeably stiff solution compared to quadratic tetrahedral or linear hexahedral [31], while the number of degrees of freedom for a linear hexahedral element is lower than for a quadratic tetrahedral (8 nodes against 10). In our case, the polycrystal was represented by cubic "grains" of equal volume, i.e. equal number of elements per grain.

The finite element program LS-DYNA was used for all simulations. The crystal plasticity material model was implemented as a user-material subroutine [32]. The subroutine utilizes an explicit integration scheme by Grujicic and Batchu [33]. Explicit integration of the momentum equations was used with mass scaling to reduce computation time.

The response of the material was studied by using a representative volume element (RVE) with periodic boundary conditions. In some cases the Taylor type homogenisation was used to reduce computation time. In this case, one element was used as an RVE and periodic boundary conditions were applied to its nodes. The tensile tests in different directions were simulated by rotating the texture around the z-axis (i.e. the thickness direction) by the appropriate angle. The texture was represented by a set of 1000 orientations, picked randomly from the total set of 2611 measured orientations. To ensure that this set represents the total texture well, several sets were picked in this way and ODFs were created for them. The difference in ODFs was insubstantial.

Several meshes with different number of elements representing each grain were tested. The corresponding stress-strain curves are shown in Figure 6, using parameters identified

below and the interaction matrix of Fivel et al. [18]. If more than 1 element per grain is used, the gradients of the stress-strain fields inside the grains may be modelled. The higher mesh resolution allows for better compatibility of the neighbouring grain deformations, relaxing the resulting local stresses and reducing the global average stress. The difference between the global response of a mesh with 8000 elements and meshes with 27000 or 64000 elements is not very large, while the computation time is roughly proportional to the number of elements. In the following, the Taylor model was used only for the identification of the parameters of the different hardening rules due to its computational efficiency. A mesh with 8000 elements was used for all other simulations where each grain was represented by 8 elements, see Figure 7.

5 Parameter identification

5.1 *Stress correction after necking*

The above described numerical setup provides the framework for uniaxial tension, where the only component of the stress tensor is the tensile stress. On the other hand, in the experiments the stress situation becomes complex after necking, with the triaxial stress field contributing to the true stress. To remove this influence and find the corrected stress, the following procedure was used. The specimen was modelled using the finite element method. The material was represented by a phenomenological plasticity model with anisotropic yield function [34] and isotropic hardening, described by a two-term Voce rule. The shape of the yield surface for the AA6060 material was found from the texture data using crystal plasticity and the full-constraint Taylor model [35]. The parameters in the Voce rule were determined through an optimization procedure using the LS-OPT software [36]. Simulation of the tension test was performed with different sets of parameters in the Voce rule. The true stress-strain curve was computed and compared with the experimental one. This was repeated until both curves were coinciding thus providing an optimum set of parameters for the Voce rule. A detailed description of the procedure is given in [37].

This procedure was used to find the corrected stress in the 90° orientation, which was taken as the reference direction. Let σ_θ denote the corrected stress at orientation θ and let ε_θ^p be the corresponding logarithmic plastic strain. Since the 90° orientation is chosen as the reference direction, we will define the equivalent stress by $\sigma_{eq} \equiv \sigma_{90}$ and the equivalent

plastic strain by $\varepsilon_{eq} \equiv \varepsilon_{90}^p$. The equivalent plastic strain for other orientations is defined from the incremental work relation

$$dw^p \equiv \sigma_\theta d\varepsilon_\theta^p = \sigma_{eq} d\varepsilon_{eq} \tag{18}$$

where σ_θ and σ_{eq} are evaluated at the same level of specific plastic work w^p .

To find the corrected stress σ_θ in other directions, the Bridgman correction [38] was used, viz.

$$\sigma_\theta = \frac{\sigma_y}{(1+2R/a)\cdot \ln(1+a/2R)} \tag{19}$$

where a is the minimum radius and R is the radius of curvature of the neck. The geometry of the neck was estimated by the relation proposed by Le Roy et al. [39], i.e.

$$\frac{a}{R} = k\left(\varepsilon_\theta^p - \varepsilon_{\theta u}^p\right) \tag{20}$$

where $\varepsilon_{\theta u}^p$ is the logarithmic plastic strain at the start of necking at orientation θ and k is a parameter. This parameter was found for the 90° direction by fitting the corrected stress-strain curve found from Equation (19) to the equivalent stress-strain curve found from the optimization procedure described above. The obtained value of $k = 0.45$ was then used for all other orientations, while $\varepsilon_{\theta u}^p$ was found directly from the directional tensile tests. The corrected stress-strain curves are presented in Figure 8.

5.2 Parameters of crystal plasticity model

The second stage of the study was to identify the parameters of the crystal plasticity model. The parameters $\dot{\gamma}_0$, μ, m and b in Equations (11)–(13) may be found in [10] and [19]. However, of principal interest here are the components of the interaction matrices $d^{\alpha\beta}$ and $g^{\alpha\beta}$ in addition to the parameter a. They were taken from different sources and may be divided into three categories. The first one proposed in [10] and [12] assumes that the latent hardening is dominating and equal for all dislocation locks. It was used in simulations of Cu behaviour but the same kind of arguments may be applied to Al as another FCC metal. The second one is the four-component interaction matrix $g^{\alpha\beta}$ in Equation (13) for the dislocation density evolution following the conclusions of Franciosi [13]. They are also usually normalized, so that the coefficient $d_5 = 1$. In both above approaches the interaction matrix in Equation (12) is reduced to one or two components (for self and latent hardening). In the third

category, both interaction matrices have six independent components. The values of the used matrices with corresponding references are given in Table 3 and Table 4. In the case of two-term Voce hardening, the self-hardening is assumed equal to unity, while the latent hardening term $q^{\alpha\beta}$, $\alpha \neq \beta$ is equal to 1.4, following the conclusions in [14]. This value is most widely used in the literature.

The remaining parameters are the work-hardening parameters K and y_c, or θ_k and τ_k ($k = 1, 2$) in the case of the two-term Voce rule, which have to be fitted to the experimental data. This was done using the optimization program LS-OPT. As described previously, it fits the output of LS-DYNA (e.g. in form of a stress-strain curve) to a target curve (in this case the experimental equivalent stress-strain curve in the 90° direction) by varying chosen parameters of the LS-DYNA simulations (in this case K and y_c or θ_k and τ_k). After calculating the mean squared error between the simulated and target curves it adjusts the parameters in such a way that the error is reduced at the next iteration. During this procedure LS-DYNA simulations are run many times, so the numerical model needs to be rather efficient, if the optimization process is to be finished in reasonable time. Therefore, the full-constraint Taylor model was used. The use of this homogenisation procedure against others, like the relaxed-constraint Taylor model and the viscoplastic self-consistent model is discussed in [40, 41].

The initial slip resistance τ_0 is assumed to be equal for all the models. It was found through the aforementioned fitting procedure, where τ_0 was the only variable, using the two-term Voce work-hardening rule – it is the most computationally efficient model – and used for all models. For this material $\tau_0 = 27$ MPa.

The results of the optimization procedure are presented in Table 5 and Table 6. One may notice that for the interaction matrices with similar structure (i.e. the 6 or 4 component matrix) the K and y_c parameters are also similar. The stress-strain curves obtained with different matrices, compared to the experimental target curve are presented in Figure 9. By varying just two parameters, it was possible to fit the crystal plasticity models to the experimental target curve, with only small discrepancies between the models with different matrices. This provides a common reference point for their comparison. Then uniaxial tension in different material directions was simulated, using these work-hardening parameters and the 8000 element mesh described above.

6   Results and discussion

To represent the in-plane anisotropy of the material, the flow stress ratio $\sigma_\theta / \sigma_{eq}$ is plotted against the orientation angle θ for given values of the equivalent plastic strain ε_{eq}. It is recalled that $\sigma_{eq} \equiv \sigma_{90}$ and further that the stresses are evaluated at the same value of the specific plastic work $w^p = \int \sigma_\theta d\varepsilon_\theta^p$. The experimental results are shown in Figure 10 for different amounts of plastic work. The plastic anisotropy of the material obviously evolves considerably from the point of yielding to fracture (which happens at strain around 100% for the 45° orientation). The general trend is that the flow stress ratio exhibits a maximum at 0° and a minimum at 22.5° at the early stages of deformation which changes into a maximum at 45° and a minimum at 0° at large deformations. One possible reason for the shift from maximum to minimum at 0° could be high initial values of the dislocation density on the slip systems activated when loading is in this direction.

The evolution of the anisotropy in plastic flow may be evaluated from Figure 5a), displaying the logarithmic strain ε_x in the width direction of the specimen against the logarithmic strain ε_z in the thickness direction of the extruded profile, or in Figure 5b) presenting the strain ratio r_y as function of tensile strain and tensile direction. It is seen that r_y differs between the different orientations at small strains, while at larger strains r_y tends to approximately unity for all orientations. This type of behaviour may be expected from a ductile polycrystal. The slip in the constituent grains has to be kinematically compatible with the extension of the specimen, which leads to grain rotations. The flow of the polycrystal is a combination of the material flow in the constituent grains, so these rotations lead to its evolution. In addition, the rotations change the resolved shear stress on the slip systems, so that new systems may activate, or the old ones may deactivate.

The flow stress ratios $\sigma_\theta / \sigma_{eq}$ obtained with crystal plasticity and different interaction matrices are compared to the experimental data in Figure 11 to Figure 16. The yield stress anisotropy (which in the current approach was assumed to be only texture dependent), i.e. flow stress ratio measured at 0.2% plastic strain, is practically the same for all models (see Figure 11), but the flow stress ratios start to diverge already at 1% equivalent plastic strain. The general trend in all the CP models is similar to the experimental one, with a minimum at the 22.5° orientation at smaller strains and a maximum at 45° for larger strains. An important difference between simulations and experiments is that the predictions, which are based on

the assumption of equal initial slip resistance and the measured crystallographic texture, generally give a lower flow stress ratio at the 0° direction than observed in the experiments. The minimum at 22.5° disappears completely from the experimental curves, but remains, though reduced, in the CP models. The maximum at 45 ° is quite overestimated by the interaction matrices after Gérard et al. [24] and Devincre et al. [23]. The simple latent hardening matrix of the two-term Voce law gives the same basic trend as the dislocation density based models.

The strain ratio r_y obtained for the different interaction matrices is compared to the experimental data in Figure 17. The variation between the responses for different models here is noticeable, but lower than the variation of the flow stress ratio. The CP models fit quite well with the experimental results both with respect to the initial value of the strain ratio and its evolution. The largest discrepancy between simulations and experiments occurs at the 0° and 45° orientations.

The results may be explained using the crystal plasticity theory for the constituent crystals of the specimen. For the most part of the aggregate the crystals undergo extension in one direction, which for most orientations may be provided by slip on one or two particular slip systems. The other deformations, namely the accommodation of deformation between different grains, have much smaller magnitude and are provided by slip of lesser magnitude on three other systems. Therefore, most of the time, the majority of slip activity is dependent only on the orientation of the crystals. This gives the resulting general trends in both stress anisotropy and strain ratio evolution which are similar for all models. On the other hand, many grains after some deformation will orient in such a way that several different slip systems may become active (the stress in these grains will reach the vertex of the crystal's polyhedral yield surface). Then, what system will get activated and what will not, depends on the evolved slip resistances of the slip systems and therefore on the latent hardening of the crystal. The slip systems that provide the accommodation of deformation of different grains may also be not unique to the crystal orientation, and will as well depend on the latent hardening description. Different slip systems activated will give variation in grain rotations and consequently strains and stresses. Therefore the models with different latent hardening matrices demonstrate some noticeable differences in plastic behaviour on the polycrystal level.

The differences on single crystal level are much more substantial. In the case of the 6-component interaction matrix, and especially the matrix of Gérard et al., the maximum local

von Mises stress, at any deformation, was more than twice as high as the global stress, while for the two-term Voce model and the 4-component matrix this difference was around 50%. The high local stresses are a result of the structure of the work-hardening rule. For the two-term Voce rule and the 4-component matrix the slip resistance of a slip system is calculated by averaging the internal variable (dislocation density or master hardening rate) on all other slip systems by lumping them all into the latent hardening category and assigning the same weight: the $d^{\alpha\beta}$ matrix for the 4-component matrix models includes either one or two independent components and $q^{\alpha\beta}$ for the two-term Voce rule includes two – for latent and self-hardening. On the other hand, in the 6-component models the influence of the slip systems on each other is much more complex, because the same 6-component matrix is used both for the dislocation density and the slip resistance calculations ($d^{\alpha\beta}$ and $g^{\alpha\beta}$ for them are assumed to be the same). In addition, for all three 6-component models considered, the proportion between the largest and the smallest component of the interaction matrix is from around 10 for the matrix of Devincre et al. to 1400 for the matrix of Gérard et al. This creates a situation where for some orientations the crystal has to slip on a certain set of slip systems (by geometrical constraint), but this set, through the interaction matrix, is hardening much faster than the same slip system sets in other grains for the same material. This leads to some peculiar behaviour, when similar responses of a polycrystal are provided by very dissimilar local plastic response. A particularly interesting question would be to prove experimentally which type of latent hardening is closer to the physical reality.

To test the validity of the hypothesis that the initial dislocation density may skew the stress anisotropy out of the texture defined pattern, simulations were performed with increased initial density on the slip system A2 for the matrices of Devincre et al. and Gérard et al. The 4-component matrix models were not used, because in these cases, the different initial dislocation densities on different slip system do not play a significant role in the anisotropy of the plastic flow for the already discussed reason of "averaging". The results are presented on Figure 12 to Figure 15. The system A2 was chosen based on some preliminary simple simulations with the full-constraint Taylor model. The initial dislocation density on system A2 was set to $3 \cdot 10^8$ mm^{-2}. The results show that indeed the initial dislocation density may increase the stress ratio in the 0° direction towards the experimental values. The interaction matrix though still controls the anisotropy development: the new stress ratios mirror the general trends of the models without the initial dislocation density, e.g. the

overshoot at 45° is still present. Therefore the hypothesis that the initial dislocation density affects the anisotropy is physically plausible.

Another difference between different latent hardening descriptions is how they behave in different methods of homogenisation. Namely in this work the full-constraint Taylor model and the CP-FEM were used. Using simple hardening rules in the crystal plasticity model, like the two-terms Voce rule, the full-constraint Taylor model gives rather accurate predictions of the global stress when compared to CP-FEM simulations [42]. However, when adopting the Teodosiu-type crystal plasticity model, the difference between the full-constraint Taylor model and even the simplest CP-FEM simulation with one linear element representing one grain becomes much more substantial, see Figure 6. As a result, the obtained values of K and y_c are not very accurate. A calibration of the material parameters using CP-FEM is possible but the increase of the computation time is large: the simulation with an 8000 element mesh took 40 times as much computer time as a simulation with the full-constraint Taylor model. In principle, the annihilation distance y_c is a physical parameter, defined mainly by the solid solution concentration in the alloy and independent of the interaction matrix. The values of y_c found form calibrations with different interaction matrices (Table 5) are mostly quite similar, but not the same. The consequence is that the hardening properties of the single crystals in the performed simulations may differ. This adds another complication in the use of the dislocation density based CP models. Nevertheless, the main point of this work still stands. When the single crystal simulation was run with different values of K and y_c but the same interaction matrix, the slip system activation pattern was the same. The activation of slip systems, and therefore the evolution of plastic anisotropy, is controlled by the interaction matrix within a broad range of K and y_c .

7   Conclusions

The AA6060 material in T4 temper was used to study the evolution of plastic anisotropy at large strains. To this end, uniaxial tensile tests in different material directions were performed with a test set-up that allowed obtaining the average true stress and the average true strain in the minimum cross-section of the sample at very high strains and until fracture. To investigate the influence of the interaction matrix on the predicted evolution of plastic anisotropy, these tensile tests were simulated with the CP-FEM, using hardening

models with different latent hardening descriptions found in the literature, and the results were compared to the experimental data.

The examined material demonstrated a continuous evolution of the anisotropy in flow stress and strain ratio that depended on the tensile direction. The CP-FEM models, using different latent hardening descriptions, all captured the general trends of this evolution quite well. On the other hand, different latent hardening matrices lead to noticeable discrepancies between the produced results, especially in the predicted evolution of the flow stress anisotropy. The discrepancies become even bigger if the local response of the constituent grains is concerned. The latent hardening description was also shown to be important if variations in the initial dislocation density are to be considered. While this type of tensile tests could hardly be used to find the values of the interaction matrix, it could well be used to assess the validity of the values found by other methods.

References

[1] Taylor GI, Elam CF. Bakerian lecture. the distortion of an aluminium crystal during a tensile test. P Roy Soc Lond A Mat 1923;102:643-667.

[2] Taylor G, Elam C. The plastic extension and fracture of aluminium crystals. P Roy Soc Lond A Mat 1925;108:28-51.

[3] Kalidindi SR, Bronkhorst CA, Anand L. Crystallographic texture evolution in bulk deformation processing of FCC metals. J Mech Phys Solids 1992;40:537-569.

[4] Peirce D, Asaro R, Needleman A. An analysis of nonuniform and localized deformation in ductile single crystals. Acta Metall Mater 1982;30:1087-1119.

[5] Tome C, Canova G, Kocks U, Christodoulou N, Jonas J. The relation between macroscopic and microscopic strain hardening in FCC polycrystals. Acta Metall Mater 1984;32:1637-1653.

[6] Weng GJ, Phillips A. An investigation of yield surfaces based on dislocation mechanics—I: Basic theory. Int. J. Eng. Sci. 1977;15:45-59.

[7] Taylor GI. The Mechanism of Plastic Deformation of Crystals. Part I. Theoretical. P Roy Soc Lond A Mat 1934;145:362-387.

[8] Kocks U. Laws for work-hardening and low-temperature creep. J Eng Mater 1976;98:76.

[9] Mecking H, Kocks U. Kinetics of flow and strain-hardening. Acta Metall Mater 1981;29:1865-1875.

[10] Teodosiu C, Raphanel JL. Finite element simulations of large elastoplastic deformations of multicrystals, Proceedings of the international seminar MECAMAT91, 1991;153-168.

[11] Hirth J. On dislocation interactions in the fcc lattice. J Appl Phys 2004;32:700-706.

[12] Delaire F, Raphanel J, Rey C. Plastic heterogeneities of a copper multicrystal deformed in uniaxial tension: experimental study and finite element simulations. Acta Mater 2000;48:1075-1087.

[13] Franciosi P, Berveiller M, Zaoui A. Latent hardening in copper and aluminium single crystals. Acta Metall Mater 1980;28:273-283.

[14] Kocks U, Brown T. Latent hardening in aluminum. Acta Metall Mater 1966;14:87-98.

[15] Franciosi P, Zaoui A. Multislip in fcc crystals a theoretical approach compared with experimental data. Acta Metall Mater 1982;30:1627-1637.

[16] Jackson P, Basinski Z. Latent hardening and the flow stress in copper single crystals. Canadian Journal of Physics 1967;45:707-735.

[17] Tabourot L, Fivel M, Rauch E. Generalised constitutive laws for fcc single crystals. Mat Sci Eng 1997;234:639-642.

[18] Fivel M, Tabourot L, Rauch E, Canova G. Identification through mesoscopic simulations of macroscopic parameters of physically based constitutive equations for the plastic behaviour of fcc single crystats. Le Journal de Physique IV 1998;8:Pr8-151-Pr158-158.

[19] Dumoulin S, Tabourot L, Gradel T, Fivel M, Moreau J. Identification of constitutive laws for Al 99.5, Advances in Mechanical Behaviour, Plasticity and Damage: Proceedings of Euromat 2000, 2000;311.

[20] Tabourot L, Dumoulin S, Balland P. An attempt for a unified description from dislocation dynamics to metallic plastic behaviour. Le Journal de Physique IV 2001;11:Pr5-111-Pr115-118.

[21] Devincre B, Kubin L, Hoc T. Physical analyses of crystal plasticity by DD simulations. Scripta Mater 2006;54:741-746.

[22] Madec R, Devincre B, Kubin L, Hoc T, Rodney D. The role of collinear interaction in dislocation-induced hardening. Science 2003;301:1879-1882.

[23] Devincre B, Hoc T, Kubin L. Dislocation mean free paths and strain hardening of crystals. Science 2008;320:1745-1748.

[24] Gérard C, Cailletaud G, Bacroix B. Modeling of latent hardening produced by complex loading paths in FCC alloys. Int J Plasticity 2012.

[25] Raphanel J, Rey C, Teodosiu C. Finite Element Simulation of the Elastoplastic Deformation of Tricrystals: Comparisons with Experiments and Analytical Solutions, in: Anisotropy and Localization of Plastic Deformation, Springer, 1991, pp. 168-170.

[26] Russell KG, Ashby M. Slip in aluminum crystals containing strong, plate-like particles. Acta Metall Mater 1970;18:891-901.

[27] Engler O, Randle V. Introduction to texture analysis: macrotexture, microtexture, and orientation mapping. CRC press, 2010.

[28] Lee E, Liu D. Finite-Strain Elastic—Plastic Theory with Application to Plane-Wave Analysis. J Appl Phys 1967;38:19-27.

[29] Norton FH. The creep of steel at high temperatures. McGraw-Hill Book Company, Incorporated, 1929.

[30] Diard O, Leclercq S, Rousselier G, Cailletaud G. Evaluation of finite element based analysis of 3D multicrystalline aggregates plasticity: Application to crystal plasticity model identification and the study of stress and strain fields near grain boundaries. Int J Plasticity 2005;21:691-722.

[31] Simonovski I, Cizelj L, Jakšić N. The influence of finite element meshes on the results of a spatial polycrystalline aggregate model. Nuclear Engineering and Design 2011;241:1184-1190.

[32] Dumoulin S, Hopperstad O, Berstad T. Investigation of integration algorithms for rate-dependent crystal plasticity using explicit finite element codes. Comp Mater Sci 2009;46:785-799.

[33] Grujicic M, Batchu S. Crystal plasticity analysis of earing in deep-drawn OFHC copper cups. J Mat Sci 2002;37:753-764.

[34] Aretz H, Barlat F. General orthotropic yield functions based on linear stress deviator transformations, AIP Conference Proceedings, 2004;712:147.

[35] Barlat F, Richmond O. Prediction of tricomponent plane stress yield surfaces and associated flow and failure behavior of strongly textured FCC polycrystalline sheets. Mat Sci Eng 1987;95:15-29.

[36] Stander N, Roux W, Goel T, Eggleston T, Craig K. LS-OPT user's manual. Livermore software technology corporation 2008.

[37] Khadyko M, Dumoulin S, Børvik T, Hopperstad O. An experimental-numerical method to determine the work-hardening of anisotropic ductile materials at large strains. Int J Mech Sci 2014.

[38] Bridgman P. The stress distribution at the neck of a tension specimen. T Am Soc Met 1944;32:553-574.

[39] Le Roy G, Embury J, Edwards G, Ashby M. A model of ductile fracture based on the nucleation and growth of voids. Acta Metall Mater 1981;29:1509-1522.

[40] Grytten F, Holmedal B, Hopperstad OS, Børvik T. Evaluation of identification methods for YLD2004-18p. Int J Plasticity 2008;24:2248-2277.

[41] Li S, Engler O, Van Houtte P. Plastic anisotropy and texture evolution during tensile testing of extruded aluminium profiles. Model Simul Mater Sc 2005;13:783-795.

[42] Saai A, Dumoulin S, Hopperstad O. Influence of Texture and Grain Shape on the Yield Surface in Aluminium Sheet Material Subjected to Large Deformations, AIP Conference Proceedings, 2011;1353:85.

8 Tables

Table 1: Chemical composition of the alloy in wt%.

Fe	Si	Mg	Mn	Cr	Cu	Zn	Ti
0.193	0.422	0.468	0.015	0.000	0.002	0.005	0.008

Table 2: Interaction matrix for FCC crystals as defined by Franciosi [15].

	A2	A3	A6	B2	B4	B5	C1	C3	C5	D1	D4	D6
A2	g_0	g_1	g_1	g_3	g_4	g_4	g_2	g_4	g_5	g_2	g_5	g_4
A3		g_0	g_1	g_4	g_2	g_5	g_4	g_3	g_4	g_5	g_2	g_4
A6			g_0	g_5	g_5	g_2	g_5	g_4	g_2	g_4	g_4	g_3
B2				g_0	g_1	g_1	g_2	g_5	g_4	g_2	g_4	g_5
B4					g_0	g_1	g_5	g_2	g_4	g_4	g_3	g_4
B5						g_0	g_4	g_4	g_3	g_5	g_4	g_2
C1							g_0	g_1	g_1	g_3	g_4	g_4
C3								g_0	g_1	g_4	g_2	g_5
C5									g_0	g_4	g_5	g_2
D1										g_0	g_1	g_1
D4											g_0	g_1
D6												g_0

Table 3: Interaction matrix for strength, Equation (11).

Parameter sets	a	d_0	d_1	d_2	d_3	d_4	d_5
Teodosiu et al. (1991) [10]	1	0.42	0.52	0.52	0.52	0.52	0.52
Delaire et al (2000) [12]	1	0.52	0.72	0.72	0.72	0.72	0.72
Tabourot et al. (1997) [17]	0.3	1	1	1	1	1	1
Fivel et al. (1998) [18]	0.3	1	1	1	1	1	1
Dumoulin et al. (2000) [19]	1	0.3	0.07	0.07	0.07	0.07	0.07
Tabourot et al. (2001) [20]	1	0.16	0.11	0.11	0.11	0.11	0.11
Madec et al. (2003) [22]	1	0.084	0.084	0.051	1.265	0.075	0.084
Devincre et al. (2008) [23]	1	0.122	0.122	0.07	0.625	0.137	0.122
Gérard et al. (2012) [24]	0.38	0.025	0.01	0.04	14.3	0.6	0.5

Table 4: Interaction matrix for dislocation density evolution, Equation (13).

Parameter sets	g_0	g_1	g_2	g_3	g_4	g_5
Teodosiu et al. (1991) [10]	0	1	1	1	1	1
Delaire et al (2000) [12]	0	1	1	1	1	1
Tabourot et al. (1997) [17]	0.2	0.3	0.3	0.3	0.4	1
Fivel et al. (1998) [18]	0.01	0.4	0.4	0.4	0.75	1
Dumoulin et al. (2000) [19]	0.2	0.8	0.8	0.8	0.8	1
Tabourot et al. (2001) [20]	0.96	0.96	0.96	0.96	0.96	1
Madec et al. (2003) [22]	0.084	0.084	0.051	1.265	0.075	0.084
Devincre et al. (2008) [23]	0.122	0.122	0.07	0.625	0.137	0.122
Gérard et al. (2012) [24]	0.025	0.01	0.04	14.3	0.6	0.5

Table 5: Calibration results for the hardening model with different interaction matrices.

Parameter sets	K	y_c [mm]
Teodosiu et al. (1991) [10]	27.755	$6.516 \cdot 10^{-6}$
Delaire et al (2000) [12]	31.767	$6.578 \cdot 10^{-6}$
Tabourot et al. (1997) [17]	7.833	$1.038 \cdot 10^{-5}$
Fivel et al. (1998) [18]	8.827	$1.044 \cdot 10^{-5}$
Dumoulin et al. (2000) [19]	12.756	$9.090 \cdot 10^{-6}$
Tabourot et al. (2001) [20]	17.824	$6.226 \cdot 10^{-6}$
Madec et al. (2003) [22]	3.606	$6.000 \cdot 10^{-6}$
Devincre et al. (2008) [23]	6.014	$5.139 \cdot 10^{-6}$
Gérard et al. (2012) [24]	5.933	$5.244 \cdot 10^{-6}$

Table 6: Calibration results for the two-term Voce hardening model.

τ_{c0}^{α}, MPa	τ_1, MPa	θ_1, MPa	τ_2, MPa	θ_2, MPa
27.00	24.85	183.81	29.17	40.95

9   Figures
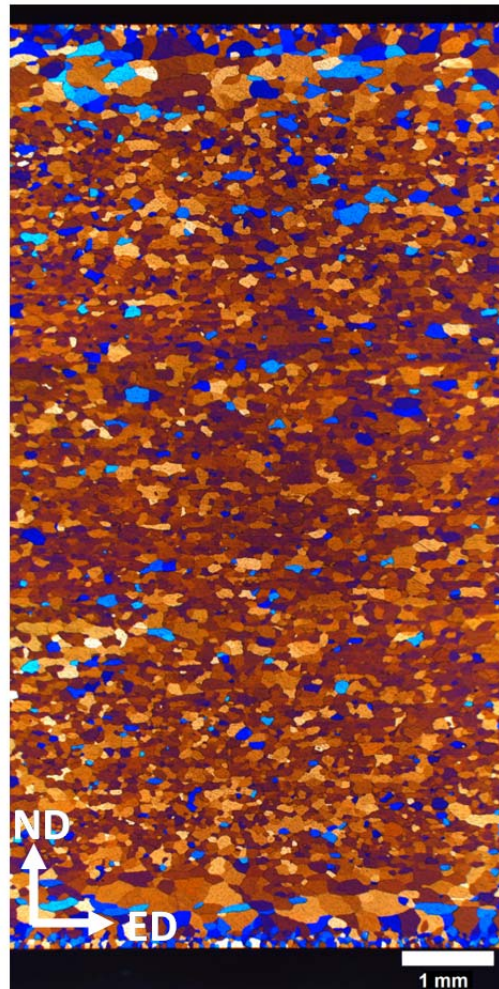
Figure 1: Grain morphology of the AA6060 alloy.

Texture Name: Harmonic: L=23, HW=5.0
Calculation Method: Harmonic Series Expansion
Series Rank (I): 23
Gaussian Smoothing: 7.0°
Sample Symmetry: Triclinic
Representation: Euler Angles (Bunge)

max = 36.802
32.000
16.000
8.000
4.000
2.000
1.000
Constant Angle: φ2

φ1 (0.0°-90.0°)

Φ (0.0°-90.0°)
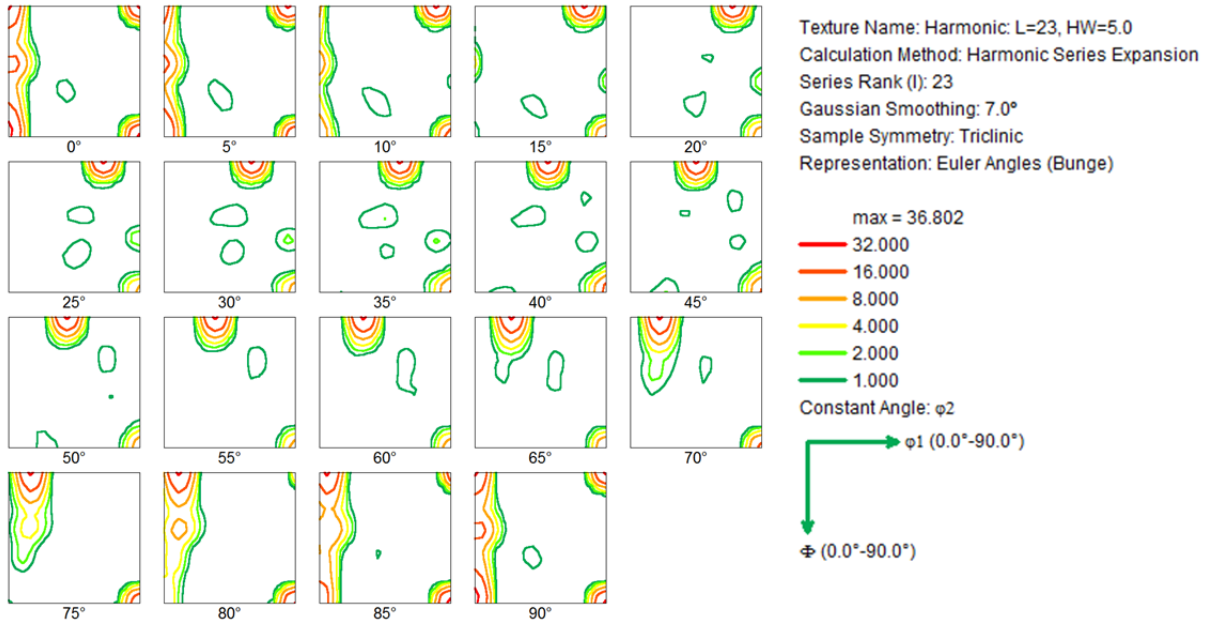
Figure 2: Orientation Distribution Function (ODF) for the AA6060 alloy
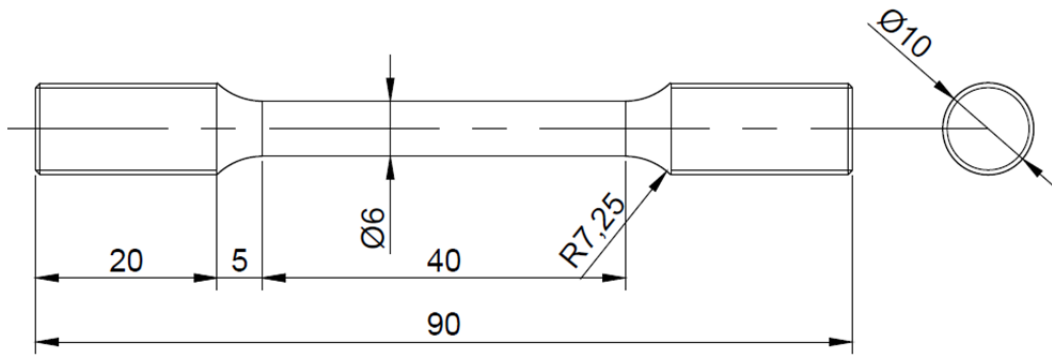
Figure 3: Uniaxial tensile test specimen geometry.
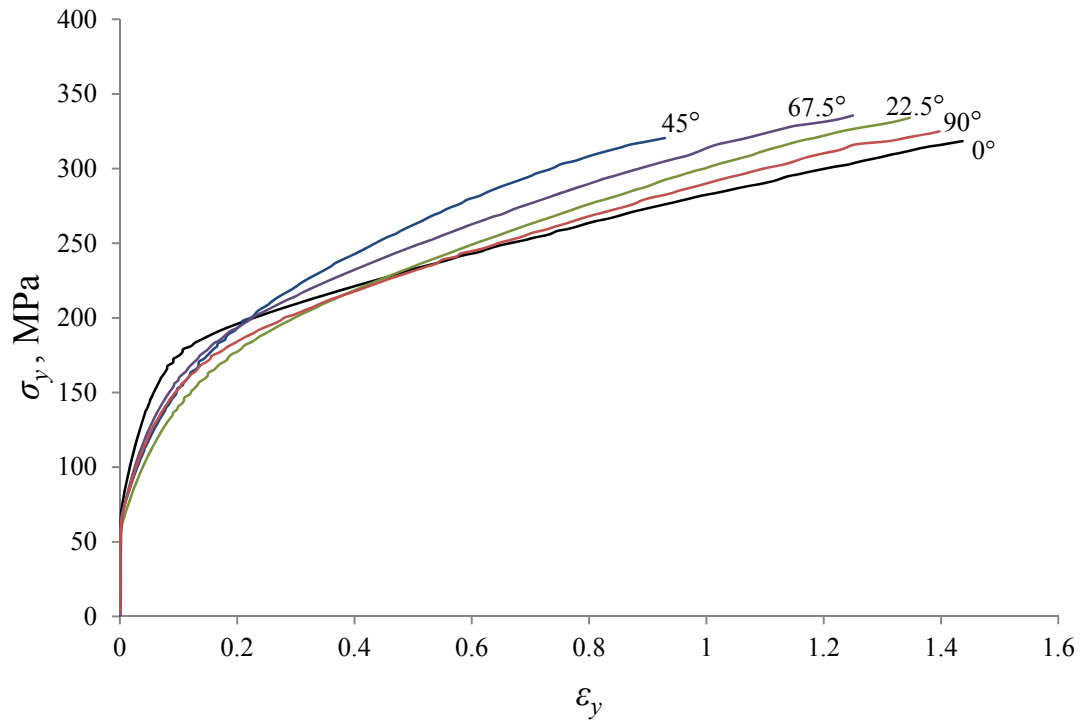
a)
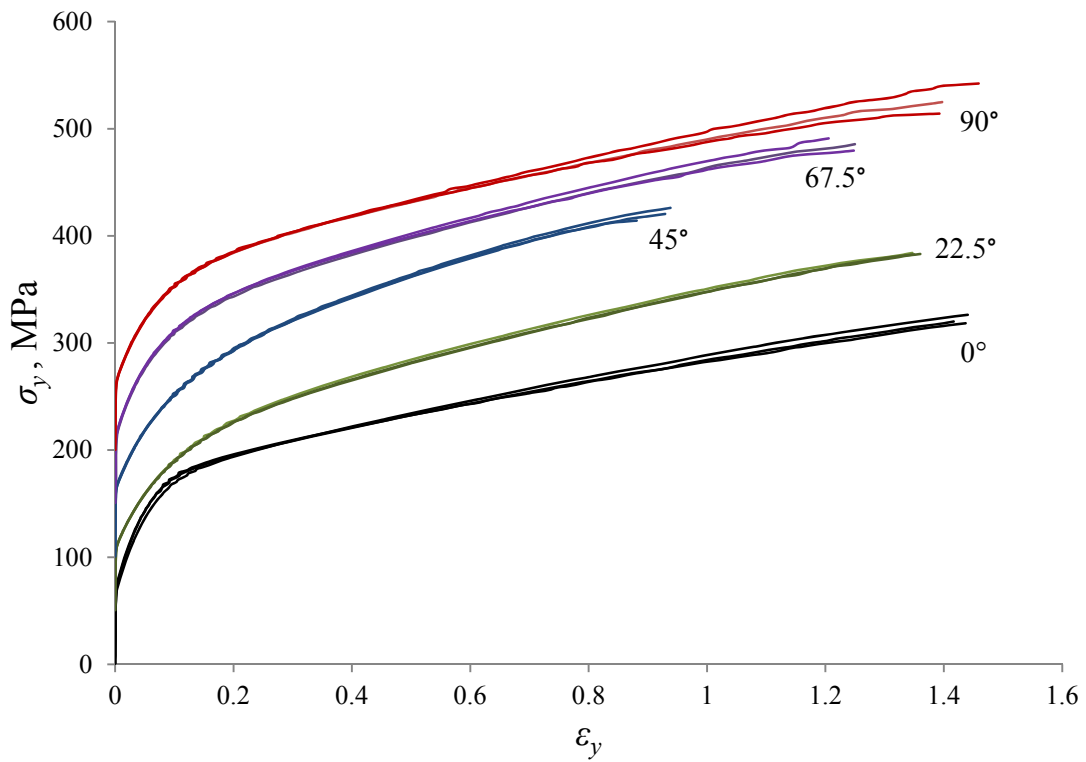
b)

Figure 4: True stress σ_y versus logarithmic strain ε_y curves for specimens with different orientations θ: a) representative curves, b) curves from all three specimens of each orientation with a 50 MPa shift between the orientations.
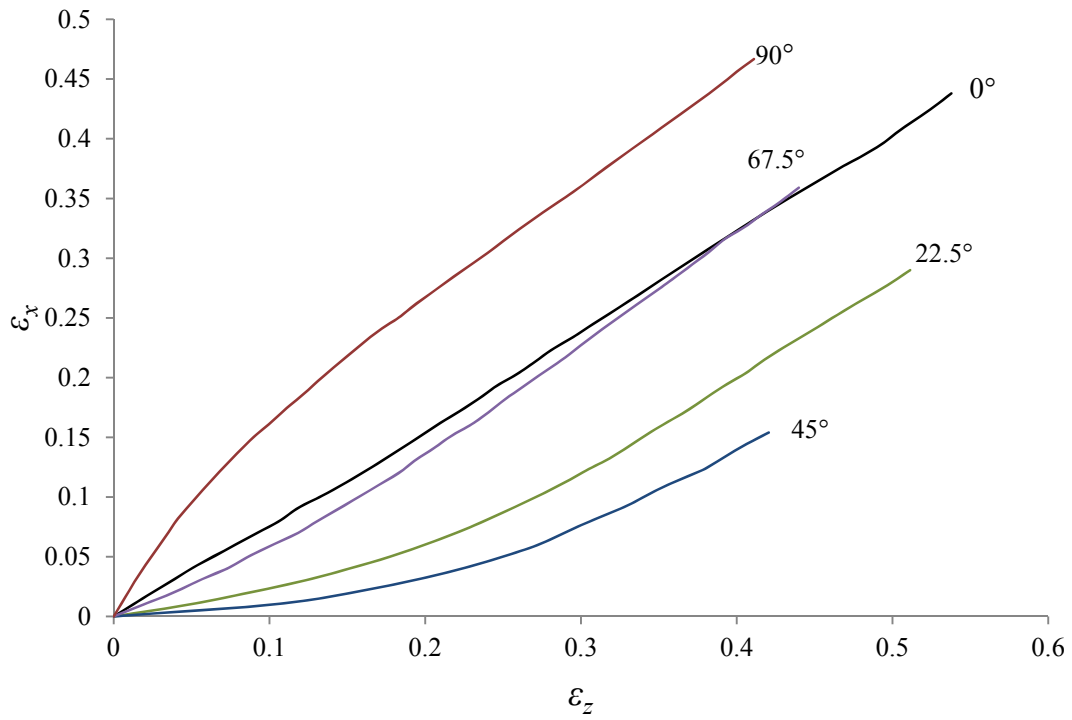
a)
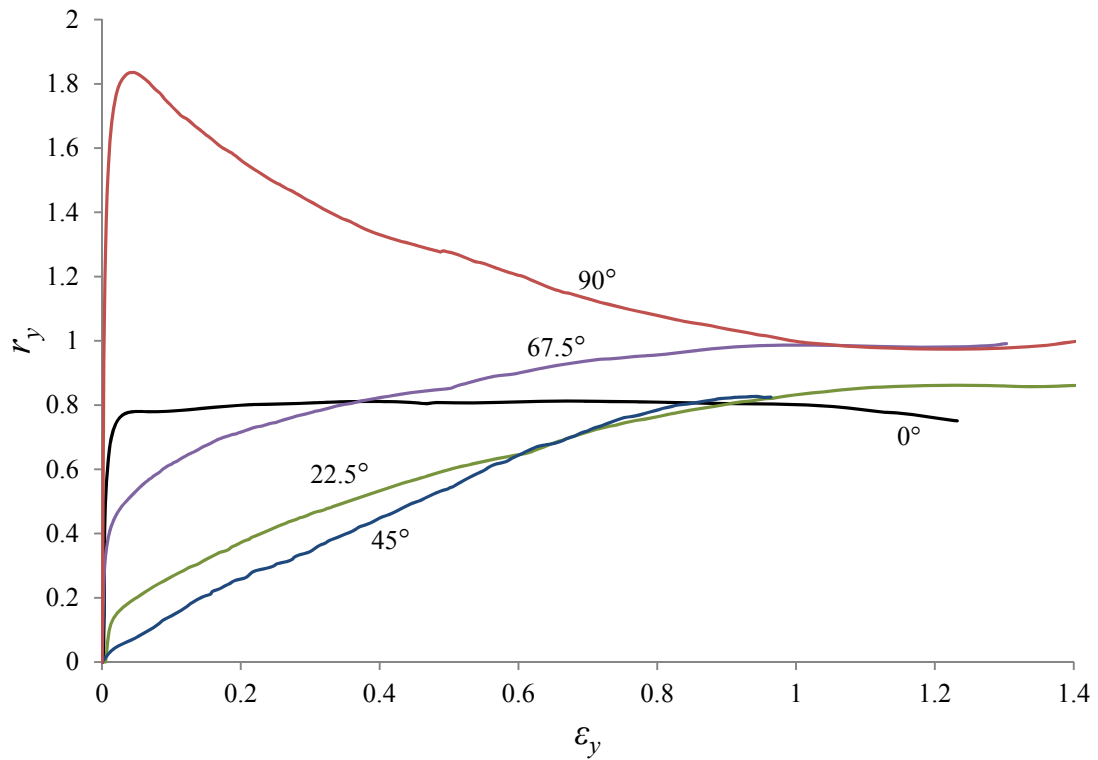
b)

Figure 5: a) Logarithmic width strain ε_x versus logarithmic thickness strain ε_z for the specimens in different directions and b) the strain ratio r_y versus longitudinal logarithmic strain ε_y.
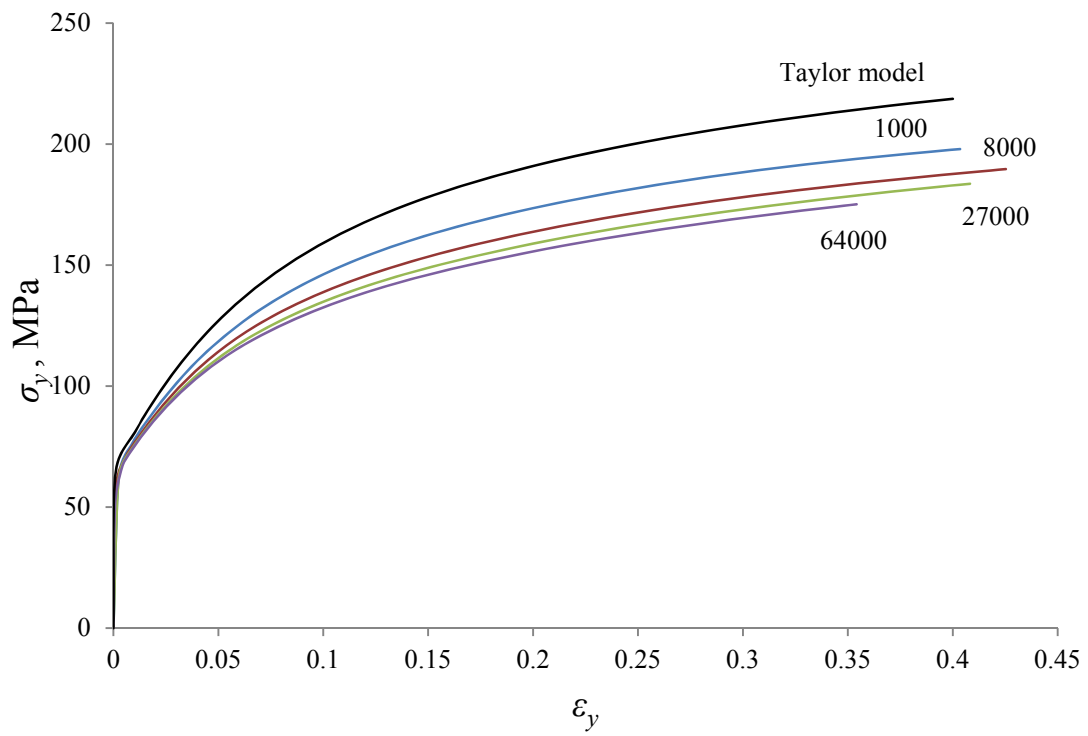
Figure 6: Stress-strain curves from FE models with different mesh resolution.
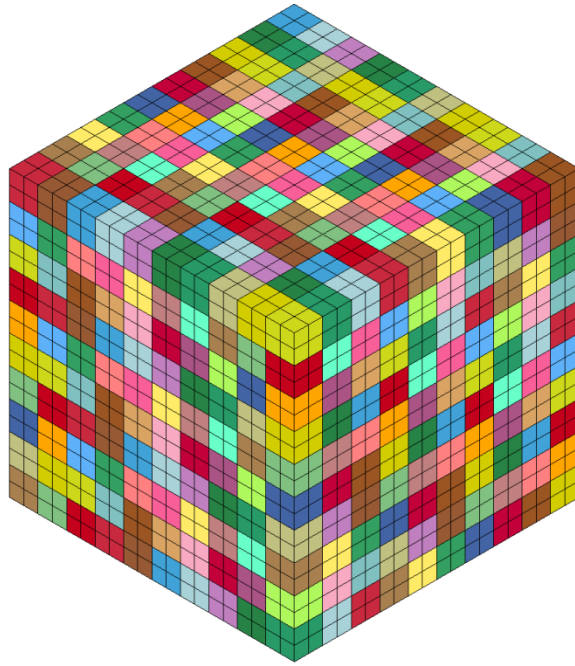
Figure 7: FE mesh with 8000 elements representing 1000 grains.
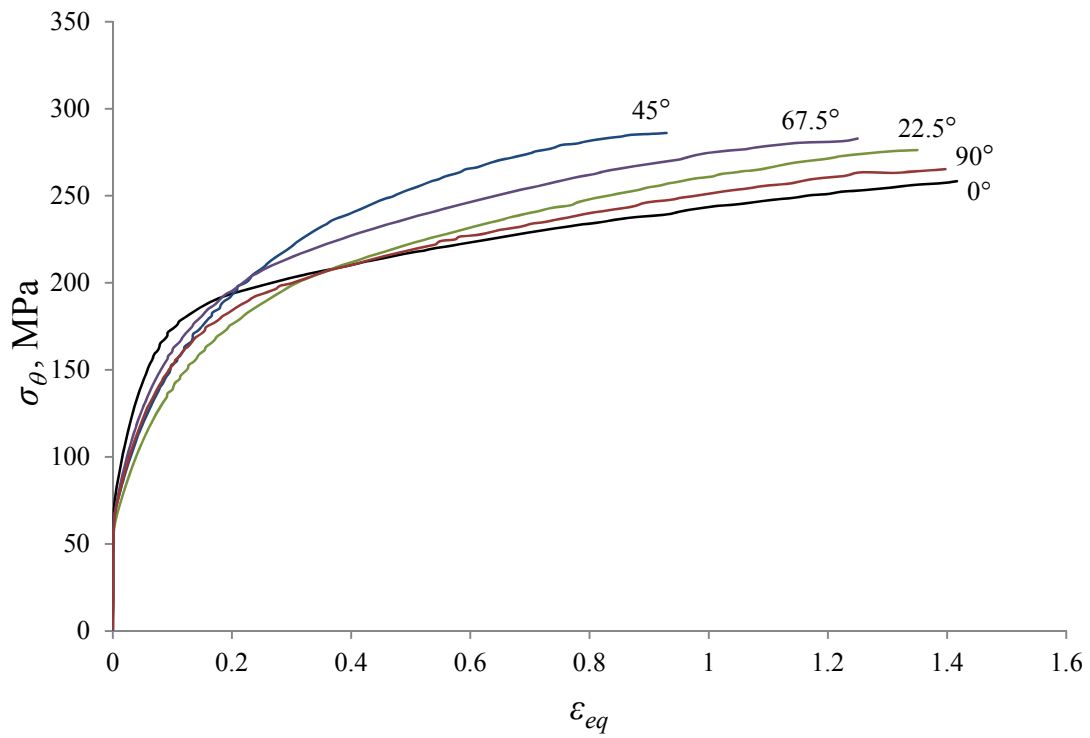
Figure 8: Flow stress (or corrected stress) versus equivalent strain for samples in different directions, where the flow stress σ_{90} at orientation $\theta = 90°$ equals the equivalent stress σ_{eq}.
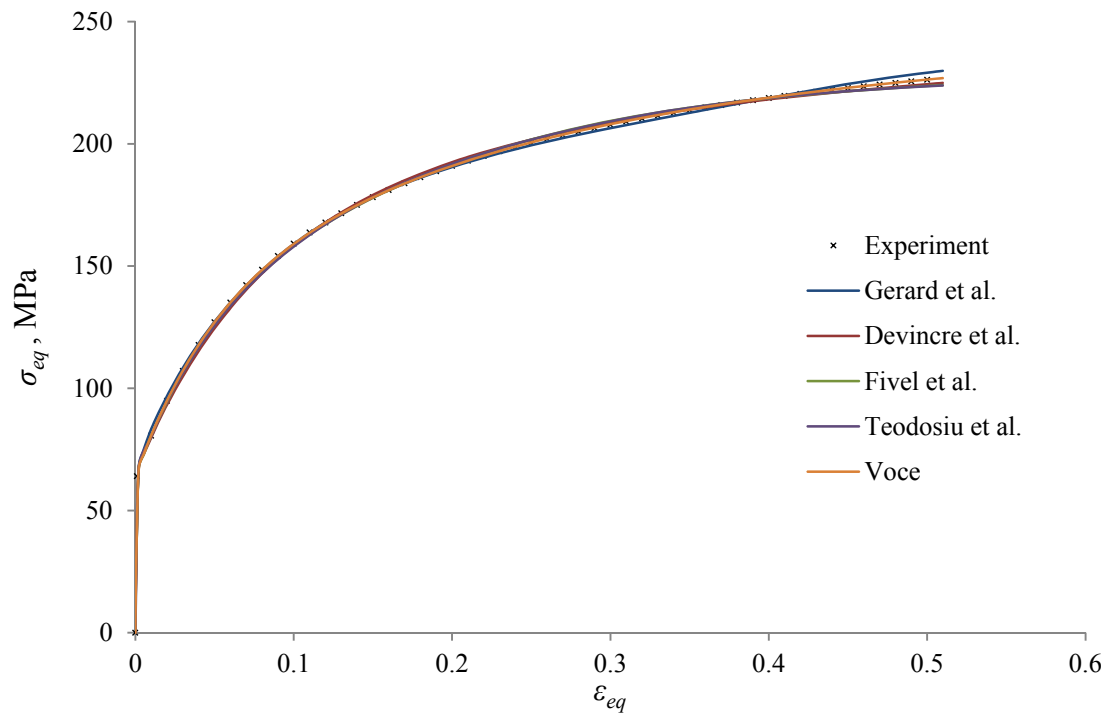
Figure 9: Calibration of the crystal plasticity model with different interaction matrices using the equivalent stress-strain curve in the 90° direction.
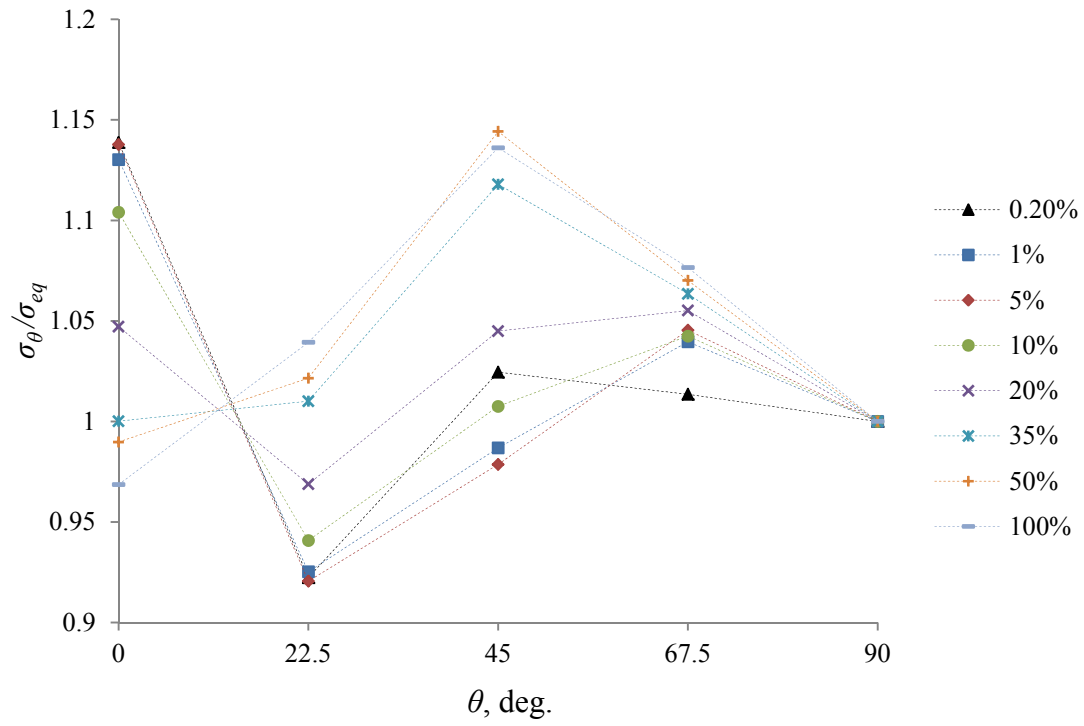
Figure 10: Flow stress ratio $\sigma_\theta / \sigma_{eq}$ from the experiment versus specimen orientation θ. The stress ratio is taken at equal values of plastic work for all directions, corresponding to the plastic strain in the reference direction, given in the legend.
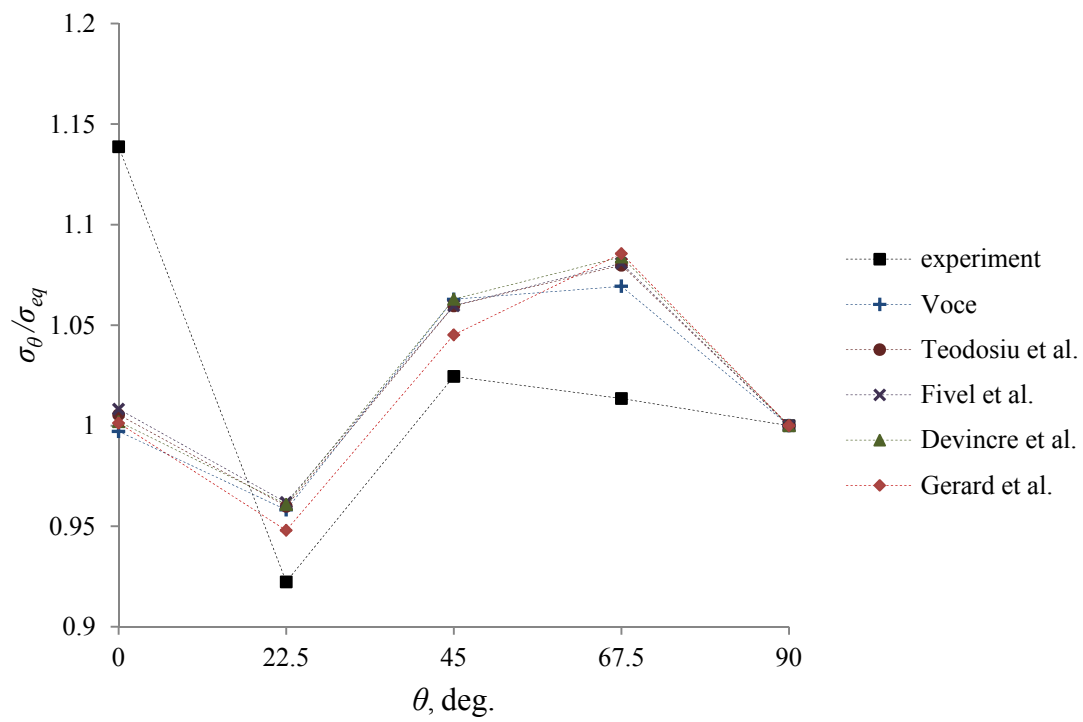
Figure 11: Flow stress ratio $\sigma_\theta / \sigma_{eq}$ at incipient yielding (0.2% plastic strain) versus specimen orientation θ from the experimental tests and simulations.
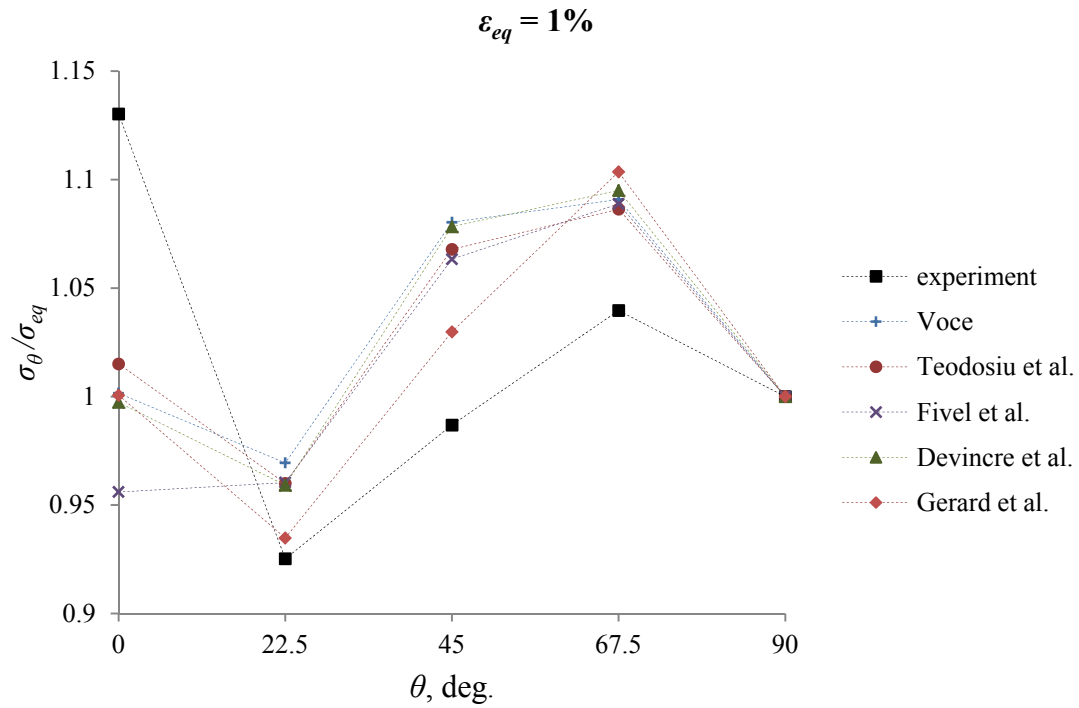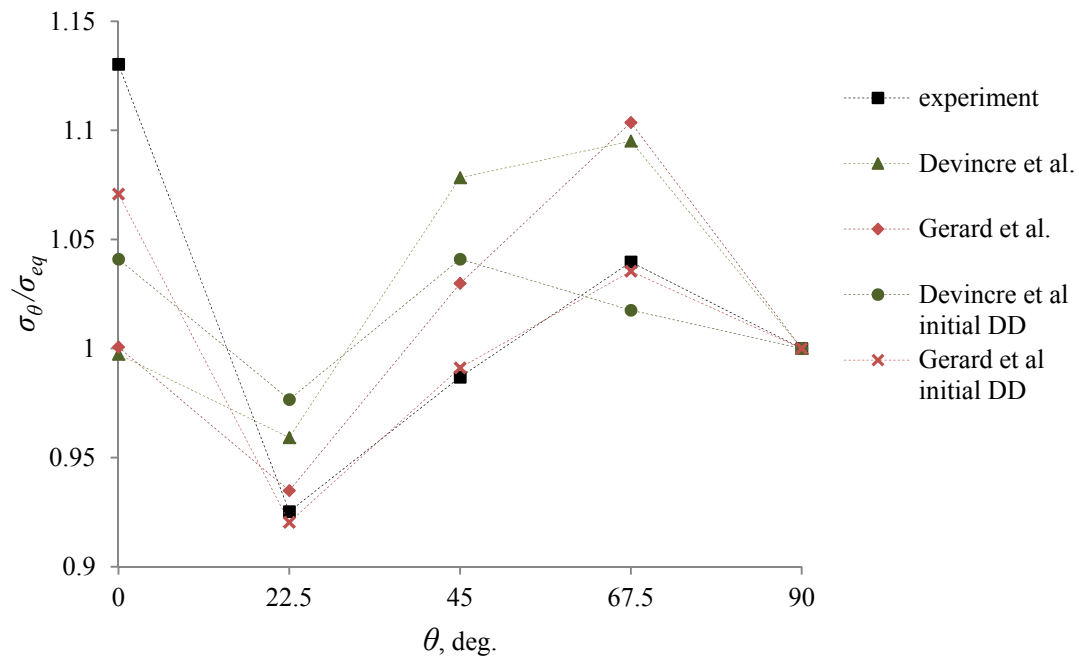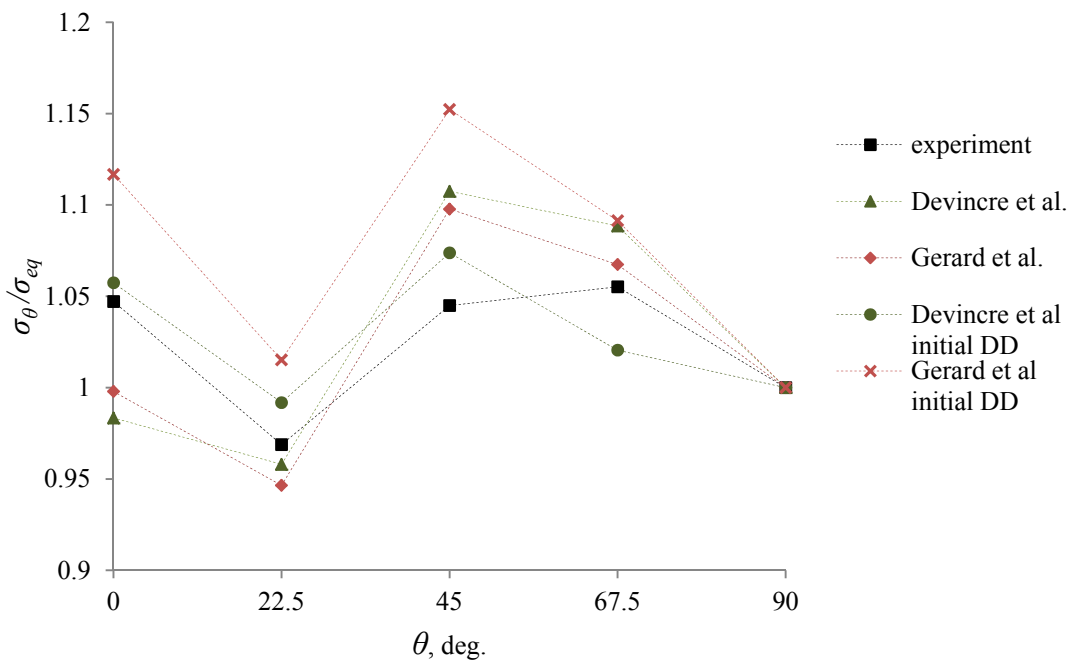
Figure 12: Flow stress ratio $\sigma_\theta / \sigma_{eq}$ against sample orientation θ for different interaction matrices at specific plastic work corresponding to 1 % plastic strain in the 90° direction. In a) the initial dislocation density is equal for all slip systems, in b) it is increased for the A2 slip system.
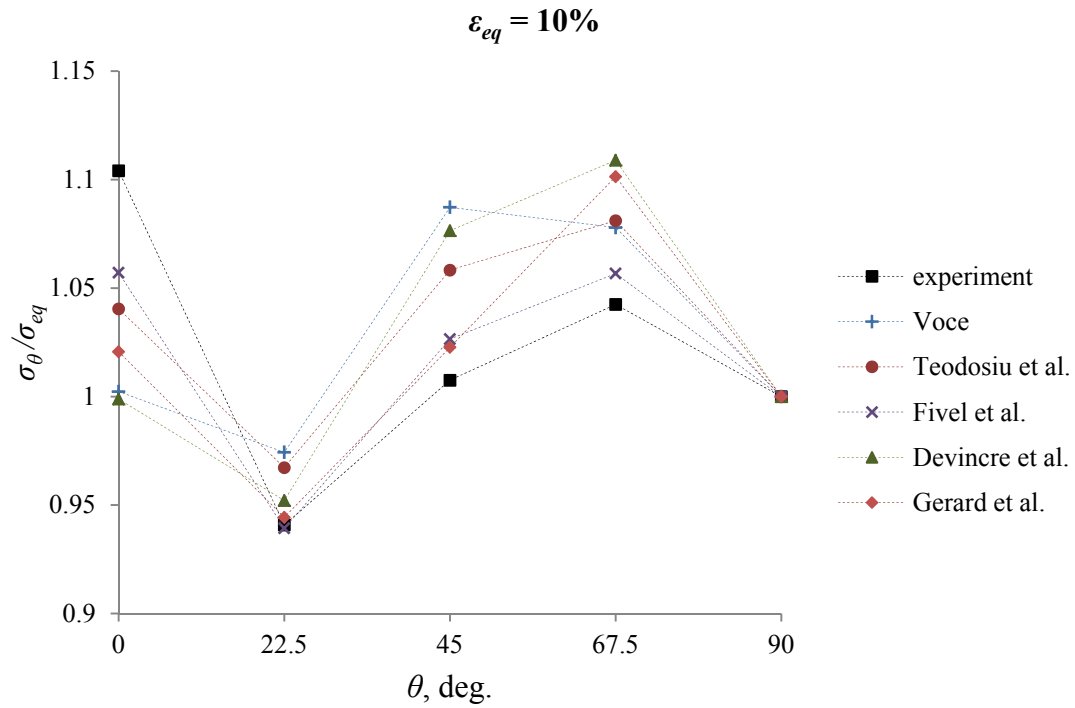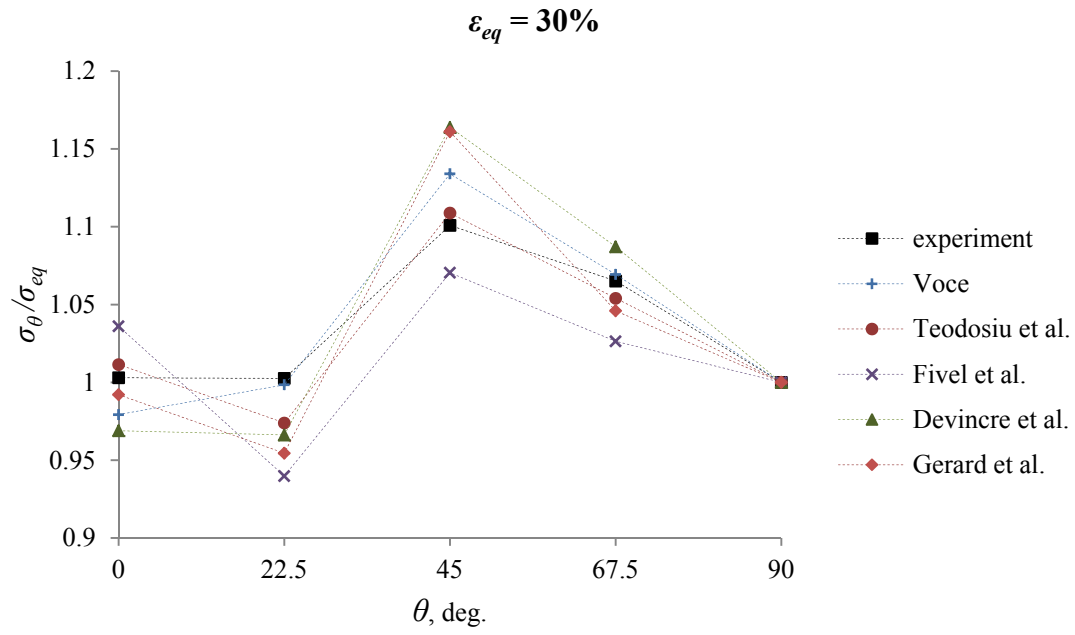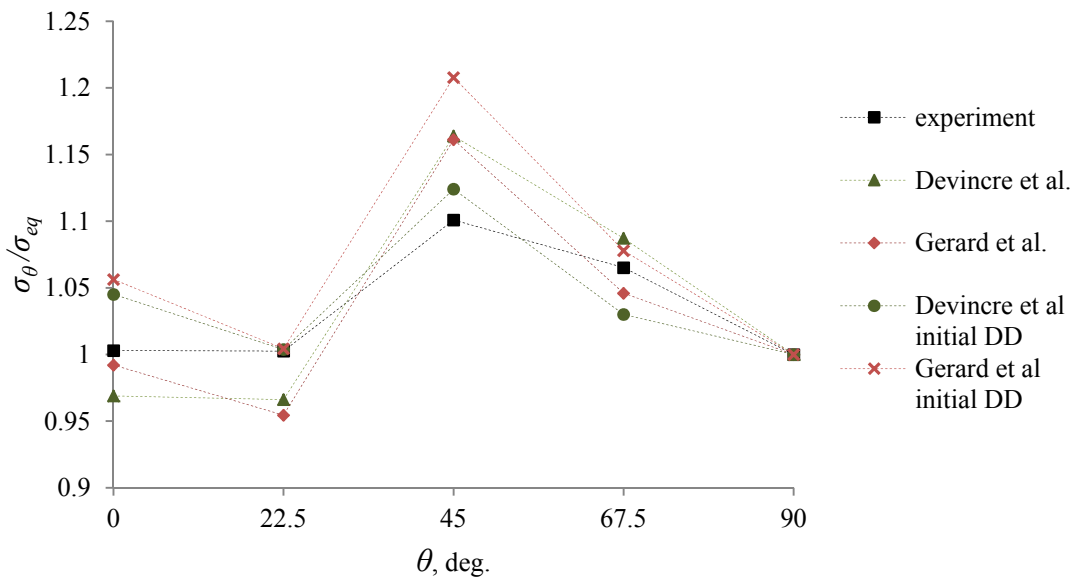
a)
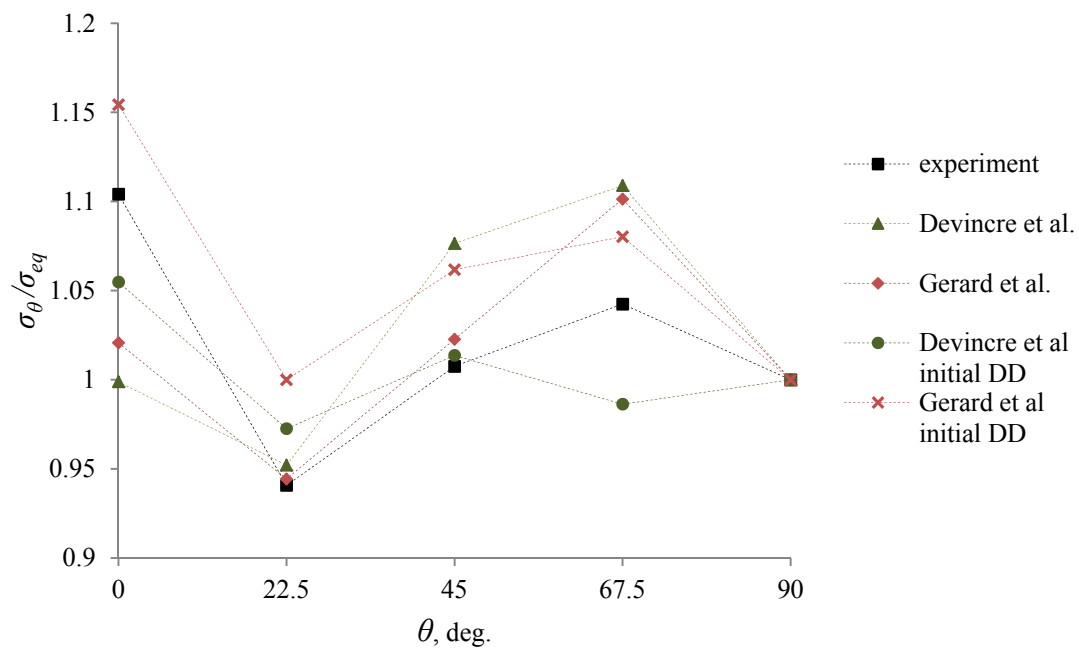
b)

Figure 13: Flow stress ratio $\sigma_\theta / \sigma_{eq}$ against sample orientation θ for different interaction matrices at specific plastic work corresponding to 10 % plastic strain in the 90° direction. In a) the initial dislocation density is equal for all slip systems, in b) it is increased for the A2 slip system.

$\varepsilon_{eq} = 20\%$
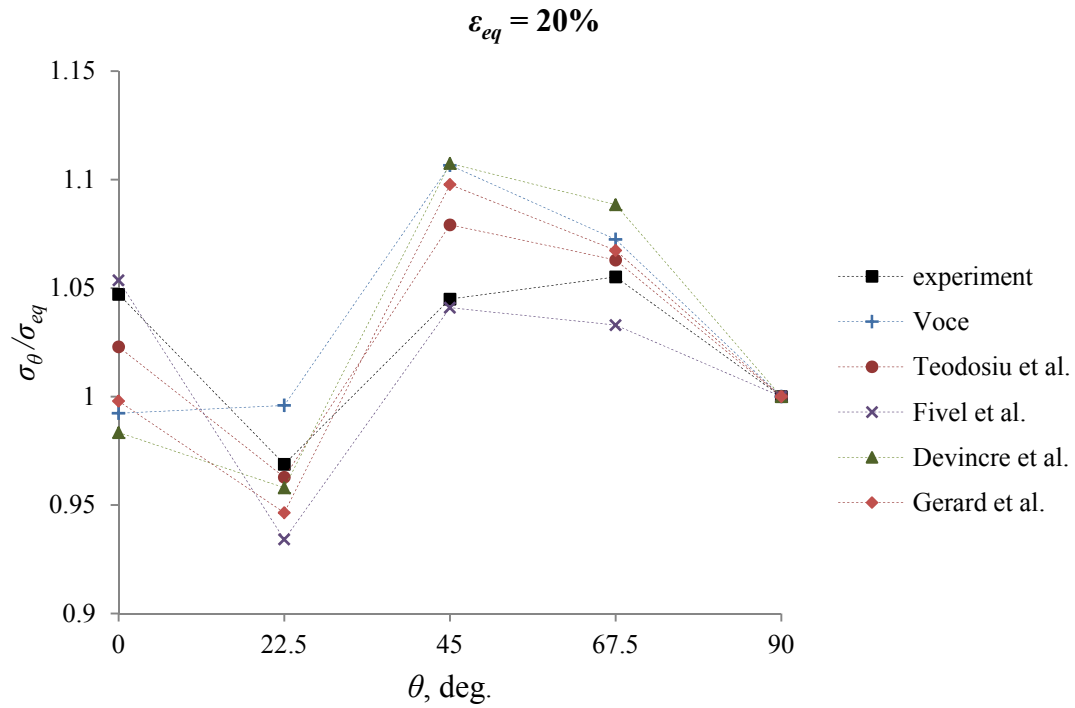
a)

b)

Figure 14: Flow stress ratio $\sigma_\theta / \sigma_{eq}$ against sample orientation θ for different interaction matrices at specific plastic work corresponding to 20 % plastic strain in the 90° direction. In a) the initial dislocation density is equal for all slip systems, in b) it is increased for the A2 slip system.

a)

b)

Figure 15: Flow stress ratio $\sigma_\theta / \sigma_{eq}$ against sample orientation θ for different interaction matrices at specific plastic work corresponding to 30 % plastic strain in the 90° direction. In a) the initial dislocation density is equal for all slip systems, in b) it is increased for the A2 slip system.
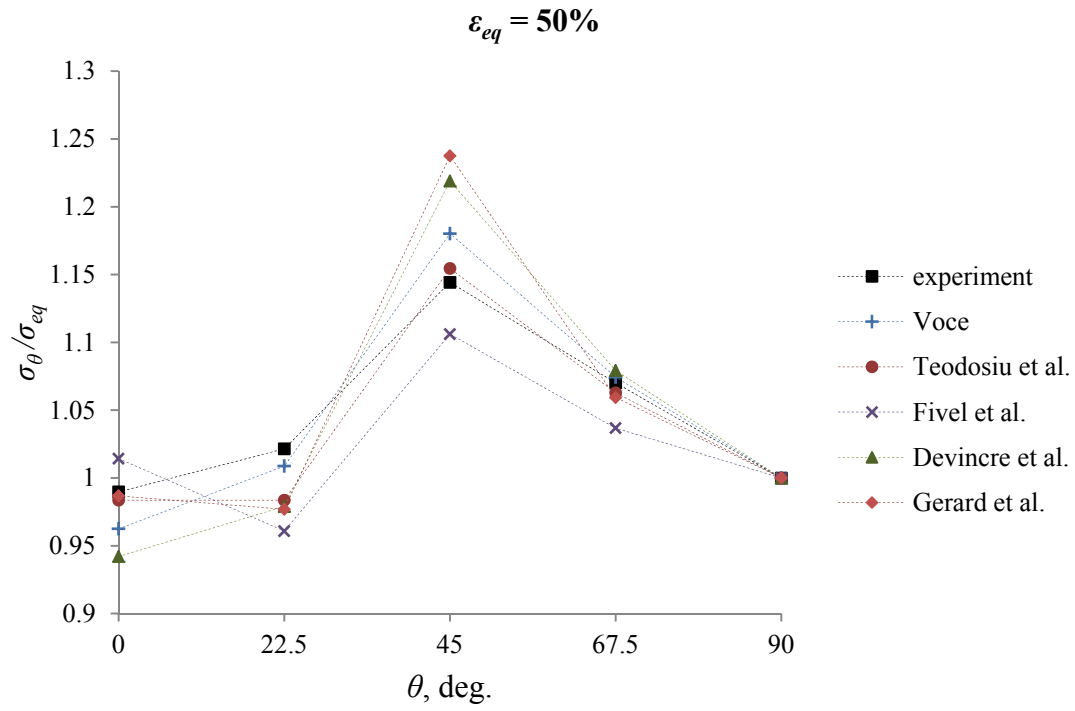
Figure 16: Flow stress ratio $\sigma_\theta / \sigma_{eq}$ against sample orientation θ for different interaction matrices at specific plastic work corresponding to 50 % plastic strain in the 90° direction.
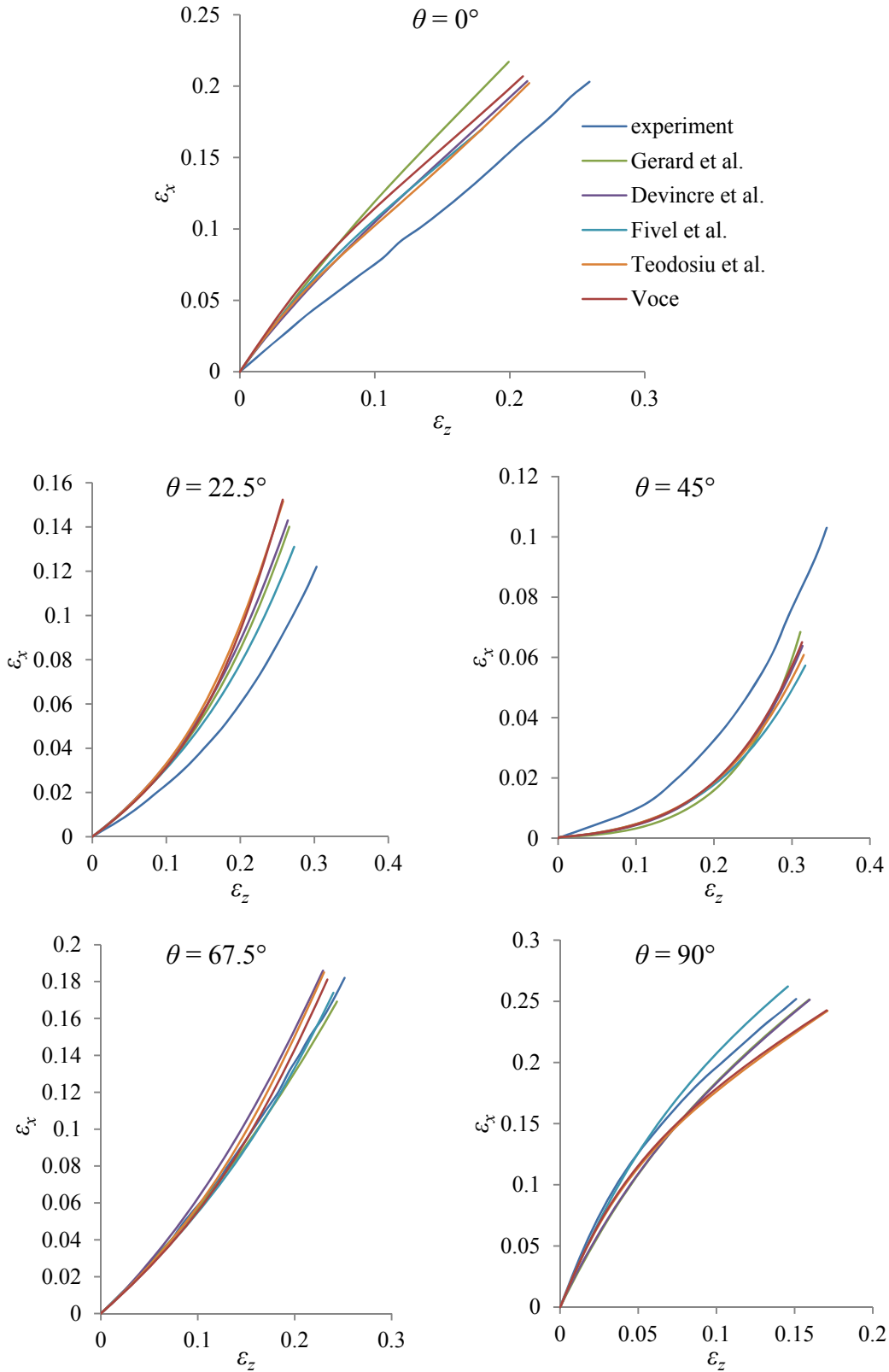
Figure 17: Logarithmic width strain ε_x versus logarithmic thickness strain ε_z for different specimen orientations θ from experiments and simulations with different interaction matrices. The slope of the curves represents the strain ratio r_y.